

# Surface Densities of Ultra-cool Dwarfs in Deep HST/WFC3 Parallel Fields: 20 L and T Dwarfs from WISPS and HST-3D

CHRISTIAN AGANZE,<sup>1</sup> ADAM J. BURGASSER,<sup>1</sup> MATHEW MALKAN,<sup>2</sup> CHIH-CHUN HSU,<sup>1</sup>  
CHRISTOPHER A. THEISSEN,<sup>1</sup> DANIELLA C. BARDALEZ GAGLIUFFI,<sup>3</sup> AND BENNE HOLWERDA<sup>4</sup>

<sup>1</sup>*Department of Physics, University of California, San Diego, CA 92093, USA*

<sup>2</sup>*Department of Physics & Astronomy, University of California, Los Angeles, CA 90095, USA*

<sup>3</sup>*Department of Astrophysics, American Museum of Natural History, Central Park West at 79th Street, NY 10024, USA*

<sup>4</sup>*Department of Physics and Astronomy, 102 Natural Science Building, University of Louisville, Louisville KY 40292, USA*

## ABSTRACT

[will fill in this after all edits]

## 1. INTRODUCTION

The structure and evolution of the Milky Way is probed by specific and homogenous populations of stars. The Milky Way stellar density profile is smooth, fit to an exponential function for the disk component and a power-law or flat spheroid for halo component (?). Ultracool dwarfs (UCDs;  $M \lesssim 0.1M_{\odot}$ ,  $T_{eff} \lesssim 3000K$ ; ?) provide a new approach for studying the Galaxy as they are abundant in every environment throughout the Galaxy. UCDs are members of the late-M, L, T and Y spectral classes, and constitute  $\sim 50\%$  of the total number of stars in the galaxy (?, ?, ?, ?). They have distinct spectra shaped by strong molecular absorption that are highly sensitive to temperature, surface gravity and metallicity. In addition, these objects do not fuse hydrogen, hence, they cool down with time. This evolution of UCDs provides potential age diagnostics that have been exploited in stellar cluster studies (???) and searches of young moving groups near the Sun (?, ?, ?, ?).

UCDs are usually discovered in red optical and infrared sky surveys (DENIS: ?, 2MASS: ??, WISE: ??, UKIDSS: ???, CFBDS: ?, Gaia: ?) but due to the intrinsic faintness of UCDs, all these samples are distance limited ( $\leq 100$  pc). Hence, efforts to constrain the luminosity function have focussed on compiling a volume-limited sample of UCDs within 20–25 pc (?????). However, UCDs cool with age; and older, metal-poor T-dwarfs populations are more dispersed into the galactic thick disk and halo (??) hinting to a possible different formation mechanism and/or initial-mass function (IMF) variations (?). A further investigation of this idea justifies searches of UCDs populations further into the thick disk and halo of the Milky Way.

Deep pencil-beam imaging and or/spectroscopic surveys provide an opportunity to characterize populations UCDs beyond the local volume and further into the halo and thick disk of the Galaxy. Early work by ? sought to investigate the dark matter content of the halo by measuring the halo luminosity function using the Hubble Space Telescope (HST) Wide Field Camera 2 (WFC2) and Planetary Camera (PC1) deep fields. They found 337 stars including 47 M dwarfs with  $M_V > 13.5$  and a turning point in power law the mass function at  $M \sim 0.6 M_\odot$  from  $\alpha = -1$  to  $\alpha = 0.44$ . Subsequent studies by ?? concluded that the contribution of low-mass stars ( $M \sim 0.3 M_\odot$ ) to the halo luminosity function is less than 1%. ? combined star-count data from shallow and deep fields and derived a scale of 800 pc and a scale length of 2500 pc, and a local density of  $10^{-3} \text{ pc}^{-3}$  for 0.2–0.8  $M_\odot$  thick disk stars consistent with a mass function  $\frac{dN}{dM} = M^{-0.5}$ . ? searched 15 deep parallel fields from the Hubble Space Telescope star-count data and estimated a scale of  $\sim 350$  pc for L & T dwarfs.

? found 17 late M, L and T dwarfs in 231.90 arcmin<sup>2</sup> of WFC3 imaging of the GOODS fields using a combination of wide and narrow-band filter colors. In addition to poor estimate of spectral types, the sample was contaminated with various non-stellar sources that could not be identified in the absence of spectral information. They estimated a disk scale height of  $290 \pm 39$  pc consistent with previous studies (??). ? identified 274 in 227 arcmin<sup>2</sup> M-dwarfs (to a limiting magnitude F125W=25) from the HST-WFC3 Brightest of Re-ionizing Galaxies (BoRG, ?) survey, using an optical and near-infrared colors and determined their spectral types using V-J color-M-dwarf subtype relation (?). They found a slightly higher density of M-dwarfs identified in the Northern fields compared to the

Southern Fields, and a disk scale-height of 0.3–4kpc with a dependence on subtype. The overall M-dwarf scale height was  $\sim 600$  pc, a number that is much larger than previous estimates mostly due to large uncertainties in the fit. ? reanalyzed these data using a Markov Chain Monte Carlo method to fit the statistic to a galactic model including a thin disk, thick disk, and halo component. They derived a scale height of  $290^{+20}_{-19}$  pc and a central number density of  $0.29^{+0.20}_{-0.13}$  pc $^{-3}$ , with no correlation of model parameters with M-dwarf subtype. This study does not probe statistics for later types. ? found 3665 L dwarfs brighter than  $z=24$  by searching 130 square degrees of the Hyper Suprime-Cam Subaru Strategic Program data. They found an average L-dwarf scale height of 340–420 pc. ? found 11,745 photometrically classified L0-T9 dwarfs distances up to  $\sim 400$  pc by searching  $\sim 2,400$  deg $^2$  of the Dark Energy Survey (DES) data. They estimated a large scale height of  $\sim 450$  pc. These last two studies provide another constraint on the number density of L dwarfs in the Galaxy using large samples ( $N > 10^3$ ); however, as in many imaging surveys, poor accuracy in spectral types significantly affects the derived parameters. Ultimately, the large uncertainties on spectral types of UCDs in imaging surveys poorly constrain their distances, and deep spectroscopic follow-up of these sources is not a priority for precious HST time.

A parallel approach is to use pencil beam sample of spectra in red optical and near infrared (NIR) with no prior selection of source type. NIR spectroscopy in particular samples the peak of UCD spectral energy distribution and broad molecular features that anchor classification schemes (e.g ?, ?). ? identified 18 M and 2 L dwarfs in the Hubble Ultra Deep Field (HUDF) and estimated their spectral types by fitting templates from ? to their Gradient-Assisted Photon Echo Spectroscopy (GRAPES) spectra in the optical wavelength regime. This study estimated a disk scale height of  $400 \pm 100$  pc for M and L dwarfs. Another study by ? used deep ACS slitless grism observations of the Probing Evolution And Reionization Spectroscopically (PEARS) fields (as part the Great Observatories Origins Deep Survey (GOODS) fields, ?) down to a  $z=25$  and spectroscopically identified 43 M4-M9 dwarfs. Using a thick and thin disk model, the study estimated a scale height for the thin disk of  $\sim 370$  pc, and  $\sim 100$  pc for the thick disk, a halo fraction between 0.00025–0.0005 consistent with previous estimates.

? discovered 3 late T dwarfs the WFC3 infrared Spectroscopic Survey ( WISPS) fields (?) identified by their strong CH<sub>4</sub> and H<sub>2</sub>O absorption features. The sample size was not large enough to put meaningful constraints on the scale height or the luminosity function of UCDs. In this paper, we expand on this study by developing an effective method to select UCDs in similar surveys.

Section 2, 3 and 4 describes the data, section 5 describes the selection process, section 6 covers the simulations and results are discussed in section 7

## 2. DATA

### 2.1. *Survey Data*

We obtain data from two pure-parallel surveys: the WFC3 Infrared Spectroscopic Parallel Survey WISPS (?) and 3D-HST ( ?, ?, ?). These two surveys used the IR channel of the WFC3 camera (?) providing low-resolution G102 ( $\lambda = 0.8\text{--}1.17\ \mu\text{m}$ ,  $R\sim 210$ ) and G141 ( $\lambda = 1.11\text{--}1.67\ \mu\text{m}$ ,  $R \sim 130$ ) grism spectra. Removal of the slit mask allows for the overlapping spectra of the  $136\times 123$  arcsec inner FOV of the WFC3 camera.

The WISP survey is a 1000-orbit HST parallel survey covering 390 fields ( $\sim 1500\ \text{arcmin}^2$ ) that follows observing programs accepted on the Cosmic Origins Spectrograph (COS) and Space Telescope Imaging Spectrograph (STIS). 3D-HST is also a parallel survey of 248-orbits spanning  $\sim 600\ \text{arcmin}^2$  as part of Hubble Cycles 18 & 19. This survey targets four extra-galactic fields: The All-wavelength Extended Groth Strip International Survey (AEGIS, ? ), Cosmic Evolution Survey (COSMOS, ?), Ultra-Deep Survey (UKIDSS-UDS, ?), the Great Observatories Origins Deep Survey (GOODS-South and GOODS-North, ?), using the ACS/G800L and WFC3/G141 grisms in parallel. Figure ?? shows an WCF3 exposure of one of fields in WISP.

Both surveys provide photometry information from various surveys and instruments in narrow and broadband filters; we use photometric data acquired using F110W, F140W, F160W filters. Figure ?? displays these filter profiles to other standard filters. We report a detailed list observations for all the fields in Table ?? as well as a sky map of all the pointings.

### 2.2. *Data Reduction*

Data reduction for the WISP survey is performed using the **AXe** software Cookbook (??) and a custom pipeline described by ?; we do perform any further reduction the both the spectroscopic data or the images provided by the survey. The data 3D-HST Survey deviates from the pipeline **AXe** pipeline and implements a full custom reduction pipeline. We use data products described by ? and the photometric catalog of sources in ? retrieved from <https://3dhst.research.yale.edu/Home.html>

### 3. SELECTION OF UCDS

#### 3.1. *F-test*

The 3D-HST survey is designed to measure accurate redshifts from emission lines, hence the spectra obtained from the data not continuum-corrected as shown in Figure ??. We obtai the correct continuum by dividing the flux of each 3D-HST spectrum by this sensitivity curve. In addition, we fitted each WISP and 3D-HST spectrum to UCDS SpeX spectra of spectral standards using  $\chi^2$  minimization following the method of ? to obtain a preliminary spectral type classification. We compared every spectrum to a straight line in the same wavelength region and measured  $\chi^2$  as

$$\chi^2(l, s) = \sum_{\lambda=1.15\mu\text{m}}^{1.65\mu\text{m}} \frac{R(\lambda) - S(\lambda)}{\sigma_s^2} \quad (1)$$

where  $R(\lambda)$  is the reference spectrum (spectral standard or line),  $S(\lambda)$  is a WISP or 3D-HST spectrum and  $\sigma_s^2$  is the noise in the WISP or 3D-HST spectrum. We use an F-test as a statical test to separate noisy/flat spectra from the rest of the sample implemented by Scipy ? as `scipy.stat.f`. A flat spectrum is defined as having  $F(\chi_s^2/\chi_l^2) > 0.5$ . We show this distribution in figure x. We use the method described in 3.4 to define UCDS candidates to be confirmed by visual inspection.

#### 3.2. *Spectral Indices*

##### 3.2.1. *Definition*

UCDs display strong  $\text{CH}_4$  and  $\text{H}_2\text{O}$  molecular features in  $1.1 \mu\text{m} < \lambda < 1.7 \mu\text{m}$  region (?), they can be separated from other stellar/galaxy populations using these features. Spectral Indices have traditionally been used to determine spectral types (?, ?, ?, ?). Thus, we defined spectral indices in five wavelength bands:  $1.15\text{--}1.20 \mu\text{m}$ ,  $1.246\text{--}1.295 \mu\text{m}$ ,  $1.38\text{--}1.43 \mu\text{m}$ ,  $1.56\text{--}1.61 \mu\text{m}$ , or  $1.62\text{--}1.67$

$\mu\text{m}$ ; denoted by H<sub>2</sub>O-1, J-Cont, H<sub>2</sub>O-1, H-Cont, and CH<sub>4</sub> respectively. Each index is the ratio of the median flux in these bands given by

$$Index = \frac{\langle F(\lambda_1 < \lambda < \lambda_2) \rangle}{\langle F(\lambda_1 < \lambda < \lambda_2) \rangle} \quad (2)$$

tracing the H<sub>2</sub>O and CH<sub>4</sub> features as well as the J and H band continuum. We measured uncertainties in each index by random sampling, assuming these uncertainties are Gaussian-distributed.

### 3.3. Training the Indices

We trained these spectral indices a on well-characterized sample of similarly-typed template UCDs. These are 1525 M7-T9 low-resolution ( $\sim 75\text{--}120$ ), NIR ( $0.9\text{--}2.5 \mu\text{m}$ ) spectra of nearby UCD templates from the SpeX Prism Library (SPL,?) with SNR  $>60$ . In addition, we use the 69 L0-Y1 UCDs from ? observed with WFC-3, and 22 Y dwarfs obtained by ? that we will refer to as the Manjavacas and Schneider datasets. We measured these indices for all these data sets, we observe an expected trend in spectral indices for similar subtypes with the changing strength of H<sub>2</sub>O and CH<sub>4</sub> features in the spectrum. We use these three data sets as a training set to to design selection criteria for UCDs candidates in WISP and 3D-HST.

### 3.4. Box Selection Criteria

We define selection criteria using boxes/parallelograms in each of 45 independent, 2D spectral index-spectral index spaces. Ideally, UCDs with similar spectral types will cluster within the same region in these spaces, away from the contaminants while the evolution of H<sub>2</sub>O and CH<sub>4</sub> bands with subtype should distinguish classes. To define the extent of each box, we fitted a central line to each of the M5–L0, L0–L5, L5–T0, T0–T5, T5–T9, subdwarf, Y dwarfs subtype groups using linear regression by minimizing  $\chi^2$ . The equation that minimizes  $\chi^2$  for a simple linear fit is given by ? as

$$\begin{bmatrix} b \\ m \end{bmatrix} = [\mathbf{A}^\top \mathbf{C}^{-1} \mathbf{A}]^{-1} [\mathbf{A}^\top \mathbf{C}^{-1} \mathbf{Y}] \quad (3)$$

where  $b$ ,  $m$  are the coefficients of the line  $mx + b$ ,  $\mathbf{Y}$ ,  $\mathbf{A}$  and  $\mathbf{C}$  are given by

$$\mathbf{Y} = \begin{bmatrix} y_1 \\ y_2 \\ \vdots \\ y_N \end{bmatrix}; \mathbf{A} = \begin{bmatrix} 1 & x_1 \\ 1 & x_2 \\ \vdots & \vdots \\ 1 & x_N \end{bmatrix}; \mathbf{C} = \begin{bmatrix} \sigma_{y1}^2 & 0 & \dots & 0 \\ 0 & \sigma_{y2}^2 & \dots & 0 \\ \vdots & \vdots & \ddots & \vdots \\ 0 & 0 & \dots & \sigma_{yN}^2 \end{bmatrix} \quad (4)$$

The values are  $x_1 \dots x_N$  and  $y_1 \dots y_N$  are the indices on the x and y-axes, and  $\sigma_{y1}^2 \dots \sigma_{yN}^2$  are the uncertainties in the y-axis spectral indices assuming Gaussian uncertainties. The choice of x-axis or y-axis are arbitrary since we do not prescribe which index is on the x-axis or y-axis but we choose all possible combinations of indices with no repetitions. The width of the box is determined by  $x_{\min, \max} = \text{median}_x \pm 3.0 \times \sigma_x$ , where  $\sigma_x$  is the standard deviation in the x-values, while the vertices of each box are defined as by  $(x_{\max}, y_{\max} = mx_{\max} + b \pm s)$  and  $(x_{\min}, y_{\min} = mx_{\min} + b \pm s)$  where  $s$  is a scatter coefficient between the line and the indices also defined as

$$s = 3 \times \sqrt{1/N \sum_{i=1}^N (y_i - (mx_i + b))^2} \quad (5)$$

This method provides a simple and automatic prescription for selecting objects within a subtype given 3 parameters  $b$ ,  $m$  and  $s$ ; we assess the effectiveness of this method by defining a completeness and contamination statistic for each of the subtype group as follows:

$$CP = \frac{TEMP_s}{TEMP_{tot}} \quad (6)$$

$$CT = \frac{WFC3_s}{WFC3_{true}} - 1 \quad (7)$$

where  $TEMP_s$  is the number of templates selected by the box,  $TEMP_{tot}$  is the total number of SpeX templates,  $WFC3_s$  is the number of WISPS and/or 3D-HST spectra selected by the box,  $WFC3_{true}$  is the number of previously known UCDs in WISPS and /or 3D-HST after visual confirmation. We only employed criteria with the lowest contamination and highest completeness to select UCDs, and all the index selection boxes are  $>85\%$  complete. We report  $b$ ,  $m$ , and  $s$  for all the possible combinations of indices in table x.

We use this selection process iteratively i.e., we first applied the best box for each subtype, that is the box with lowest contamination and highest completeness, we visually inspected the selected spectra, updating  $WFC3_{true}$  through this step. We then recomputed CT and CP for all the boxes and repeat this process until there were no new candidates. As a final step, after all selection has been applied, we visually inspected at all the 1986 candidates to find any objects missed by spectral indices, we further discuss the effects of our selection process in section ???. The best criteria for each of the subtype groupings are summarized in table x.

### 3.5. Spectral Classification and Visual Inspection

After visual inspection of the all the candidates and removal of remaining contaminants, we compiled a sample of UCDs with accurate spectral types. To determine the spectral type classification of each UCD, we compared each of WISP& 3D-HST UCD to SpeX spectral standards using the lowest  $\chi^2$  statistic following the procedure of ?.

In addition to spectral types, we computed photometric distances for all the UCDs using absolute 2MASS J and H relations from ?. Given that these relations are defined for J and H filters, we inferred similar relations for F110W, F140W, F160W filters using the following steps: we first computed an offset between 2MASS J and H magnitudes and AB Hubble magnitudes <sup>1</sup> by convolving the a SpeX standard for that spectral type with the respective filter. This offset in convolutions is then added to the absolute magnitude-spectral type relations in 2MASS J, H filters to obtain the new relation in Hubble filters. We used these relations throughout this study to determine distances given an apparent F110W, F140W or F160W magnitude and a spectral type.

### 3.6. Random Forest Classifier

As an alternative to fitting to spectral to an arbitrary cutoff using an F-test, we trained a random forest classifier by deploying `RandomForestClassifier` implementation by `scikit-learn` ? to classify potential UCDs. Random forests have been shown to reliably predict M-dwarf subtypes based

<sup>1</sup> 3D-HST F140W and F160W magnitudes are computed using reported fluxes in photometric catalogs in ? as  $-2.5 \log_{10} F + 25$ , while WISPS magnitudes are used as reported



on colors (?). The training set is composed of spectral templates defined in 3.3 and a list of 20 UCDs visually confirmed and selected by F-test cutoff and the method described in 3.4. The total number of objects in the training set is 3610, made of 1856 visually confirmed non-UCDs, 1525 SpeX templates, 77 objects from the Manjavacas set, and 22 objects from the Schneider set. We used a set of 15 features including all 10 spectral indices as proxy for color, the signal-to-noise ratio in the J-continuum (SNR-J), the two  $\chi^2$ s and their ratio, and the F-test value. We used two labels: UCD, and non-UCD to describe ultracool dwarfs and the rest of the set. We split the training set and the test set as 50% and 50% and achieved an accuracy score of 94.8% in cross-validation. We show the confusion matrix in figure x. We predicted labels for the 74913 spectra with SNR-J >3 in WISP & 3D-HST. 601 are labelled as UCDs while 74312 are labelled as non-UCDs. We then proceeded with steps and visual confirmation to select L0-T5 candidates.

## 4. RESULTS

### 4.1. *M, L, T Dwarfs Candidates*

We found 20 L, T dwarfs. We purposely excluded M-dwarfs in the sample given that H<sub>2</sub>O and CH<sub>4</sub> features in these regions are weak. We report their distances and photometry in table xx. We found L-dwarfs up to  $\sim 1000$  pc, and T-dwarfs up to  $\sim 500$  pc; the distribution of distances for all the UCDs is shown in Figure ?. We recovered the 3T-dwarfs discovered by ?

#### 4.1.1. *L Dwarfs*

#### 4.1.2. *T dwarfs*

### 4.2. *Comparison to Predictions*

#### 4.2.1. *Brightness and Faintness limit*

We aim to constrain the number density of UCDs; an accurate estimate of the effective distance/volume of each pointing is crucial. ? reported the effective depths of all the pointings in 3D-HST, however, given the SNR cut, we expect the a brighter limit than these reported depths. Hence, we adopted higher faintness limits of F110W=22.5, F140W=22.6, F160W=22.7 following the peak of the distribution of magnitudes (Figure ??) for all sources satisfying the SNR cut and we used

mag=18 as the brightness limit of all the fields in all three filters. We then converted these faint and bright F110W, F140W and F160W into near and far-distances for each spectral type, using the absolute magnitude vs spectral type relation from ? (similar to distances in section ??).

#### 4.2.2. *Selection Function*

Because we applied several selection criteria to narrow down our sample for visual confirmation, it is possible we may have missed a few UCDs in the WISPS/3D-HST fields; particularly low SNR or peculiar objects due, in part, to uncertainties in spectral indices. To fully quantify these effects, we generated a distribution of spectra uniformly sampling our SNR distribution across a wide range of SNRs and measured their recovery rate through this selection process. We first selected a sample of 20 highest SNR objects in the SpeX sample (Figure x), and added  $10^3$  iterations of Gaussian noise to these spectra until the overall SNR to noise in the spectrum is reduced to the SNR-J limit of 3.0. We then applied our selection processes to this sample of simulated spectra by measuring spectral indices and applying first f-test criterion where  $F(\gamma) \geq 0.5$  and then the box index-index selection criteria. The fraction of spectra selected per spectral type per SNR bin is defined as the probability of selection of an object within that SNR-J and SpT range. Hence it a close representation of our selection bias. Ideally, we would simulate a homogeneous distribution of spectra from theoretical models and place them at a range of distances throughout the Galaxy as observed through the instrument; we would then apply our selection criteria to quantify our selection effects. However, such an exercise would present a difficult task and introduce new biases in the analysis. We therefore defined the selection function as

$$\mathcal{S}(\text{SNR-J}, \text{SpT}) = \frac{N_s}{N_{tot}}$$

where  $N_s$  is the number selected spectral type and SNR bin, and  $N_{tot}$  is the total number of objects in that bin.

#### 4.2.3. *Number Densities*

We compared the number densities measured in these two surveys with expected densities given a simple model that incorporates our selection function through the following steps:

1. We first simulated a sample of  $10^5$  UCDs in a power law mass function for a range of masses  $0.02 M_\odot$  and  $0.15 M_\odot$  as

$$\frac{dN}{dM} = \left( \frac{M}{M_\odot} \right)^{-0.6} \quad (8)$$

normalized to  $0.0055 \text{ pc}^{-3}$  at  $M=0.10 M_\odot$  (, ); we assigned each of these UCDs an age drawn from a uniform age distribution spanning 100 Myr–10 Gyr. We then assigned a temperature using evolutionary models from . Finally, using temperature -spectral type relation from , we converted temperatures to spectral types. We defined  $\Phi(\text{SpT})$  as this normalized distribution of spectral types.

2. To account for the effect of galactic structure, we computed an effective volume for each spectral type defined following ? defined as

$$V_{eff}(\text{SpT}) = \frac{1}{3}(d_{max}^3 - d_{min}^3) \times \Delta\Omega \times V_c \quad (9)$$

. Where  $\Delta\Omega$  is the solid angle of the pointing and  $d_{max,min}$  are the effective maximum or minimum distances given by

$$\log d_{min,max} = \frac{1}{5}(m - M_J(\text{SpT})) + 1 \quad (10)$$

.  $V_c$  is a volume correction term, to account for the galactic structure obtained by integrating the galactic density as

$$V_c(l, b) = \frac{\int_0^{\delta x} \rho(x, l, b) x^2 dx}{\int_0^{\delta x} \rho_0 x^2 dx}$$

where  $x$  is the 3D- galacto-centric distance in along the line of sight of the field, and  $\rho(x)$  is the galactic density along that line of sight. We set  $\delta x = d_{max} - d_{min}$  as the total depth of a given pointing. We assumed a standard galactic structure model similar from . The spatial density of stars in each pointing is given by

$$\frac{\rho(R, z)}{\rho_0} = \exp\left(-\frac{|z - Z_\odot|}{H_{thin}}\right) \times \exp\left(-\frac{R - R_\odot}{L_{thin}}\right) + f_{thick} \exp\left(-\frac{|z - Z_\odot|}{H_{thick}}\right) \times \exp\left(-\frac{R - R_\odot}{L_{thick}}\right) + f_{halo} \left( \frac{R_\odot}{\sqrt{R^2 + (z^2/q^2)}} \right)^{-p}$$

$H_{thin}, H_{thick}$  are the scale height of the thin and thick disk,  $L_{thin}, L_{thick}$  are the scale length of the thin/thick disk,  $q$  is the axial ratio the halo sphere,  $p$  is the flattening parameter and  $f_{thick}, f_{halo}$  are the fraction of stars in the thin thick disk and the halo.

3. Given that our selection function is a function of both SNR-J and spectral type, we must assign a SNR-J to the distribution of 10,000 simulated objects. We computed a distribution of distances where the probability is given by

$$P(d_{min} < d < 2 \times d_{max}, l, b) \propto d^3 \times V_c(l, b) \quad (11)$$

where  $l, b$  are galactic latitude and longitude.

4. After assign each simulated UCD a distance, we computed an apparent magnitude using a polynomial to fit log SNR-J to the absolute apparent magnitudes of the WFC3 UCD sample (Figure x).
5. We then used our selection function  $\mathcal{S}$  to assign a probability of selection to each of the UCDs
6. The expected number of sources per spectral type is given

$$N_{exp}(SpT) = \rho_0 \times V_{eff}(SpT) \times \sum_i \mathcal{S}_i n_i(SpT) \quad (12)$$

. Where  $n_i$  is the number of objects in a spectral type bin and  $\mathcal{S}_i$  is the probability of selection for each object in that spectral type bin. I can't Figure out how to write an equation saying that I grouped the objects that assigned probability by spectral type then summed those probabilities We compare these numbers to the observed numbers of UCDs in Figure x

## 5. SUMMARY & DISCUSSION

We have presented a method for selecting UCDs in deep HST surveys using spectral indices. This method could potentially be applicable to other infrared surveys that are contaminated with UCDs. We notice that our contamination statistic are relatively high but they can be greatly reduced by eliminating the lowest SNR sources from the sample. This method is not effective for selecting very

low SNR sources due to large uncertainties in spectral indices (SNR-J<3.0) and early M-dwarfs as the absorption features in these wavelength ranges are shallow.

The number of T-dwarfs is consistent with expectations given atmospheric cooling effects (?) from evolutionary models. As UCDs age, they quickly pile up on at the lower end of the spectral type distribution and cooler temperatures. ? estimated a change in scale height of ( $\Delta H \sim 50$  pc) in the mid-L dwarf regime by comparing galactic models for different cooling scenarios; while the scale height in for M-dwarf remains constant independent of subtype. Despite the high accuracy in spectral types for the sample of UCDs presented in this study, the small sample of size of 20 could not accurately constrain the scale height for each spectral type.

Moreover, the L/T transition region is sensitive to unresolved binaries (?). ? shows that given a spectral binary fraction of  $\sim 10\%$ , the surface densities for volume-limited sample of primaries and combined systems are similar but present a slight bump ( $\Delta \Sigma \lesssim 5 \times 10^{-5} \text{ deg}^{-2}$ ) for early T dwarfs. Given our total search area of  $\sim 0.58 \text{ deg}^2$ , we do not expect a significant effect of the spectral binary fraction to the reported densities, hence we assumed that none of the UCDs in this study are unresolved binaries in our simulation.

Metallicity effects affect the number of subdwarfs we expected in this sample. UCDs in the thick disk and the halo have similar kinematic ages with stellar populations in these parts of the Galaxy; and UCDs at different metallicities follow different evolutionary tracks. L subdwarfs in the local neighborhood are therefore rare, and this study does not significantly probe large volumes in the thick disk and halo. ? found  $0.04 \times \text{deg}^{-2}$  L subdwarfs in the UKIDSS/SDSS fields; in fact, we expect the number of subdwarfs to be  $\sim 400$  times lower than the expected number of dwarfs in the sample. Given that we only searched  $\sim 0.58 \text{ deg}^2$  of the 3D-HST fields, it is not surprising that we did not find any subdwarfs in the sample.

Future space missions such as JSWT, Euclid will be contaminated by UCDs. ? predicted that the number density of UCDs (M8–T8) in JSWT fields peaks around J $\sim 24$  mag with a total surface density of  $\Sigma \sim 0.3 \text{ arcmin}^{-2}$ . With the *Large-Scale Synoptic Telescope* (LSST), and the *Wide-Field Infrared Survey Telescope* (WFIRST), we expect in increase in both sample size and spectral type

accuracy, expanding the parameter space necessary to put significant constraint on the star formation history of the Milky Way in general and the mass function of UCDs in particular (?, ?).

### Acknowledgement for WISPS

This work is based on observations taken by the 3D-HST treasury program (GO 12177 and 12328) with the NASA/ESA HST, which is operated by the Association of universities for Research in Astronomy, Inc. under NASA contract NAS5-26555.

CA thanks the LSSTC Data Science Fellowship Program, which is funded by LSSTC, NSF Cyber-training Grant #1829740, the Brinson Foundation, and the Moore Foundation; his participation in the program has benefited this work.

*Software:* Astropy(?), Matplotlib, SPLAT(?), Scipy, Pandas, Seaborn

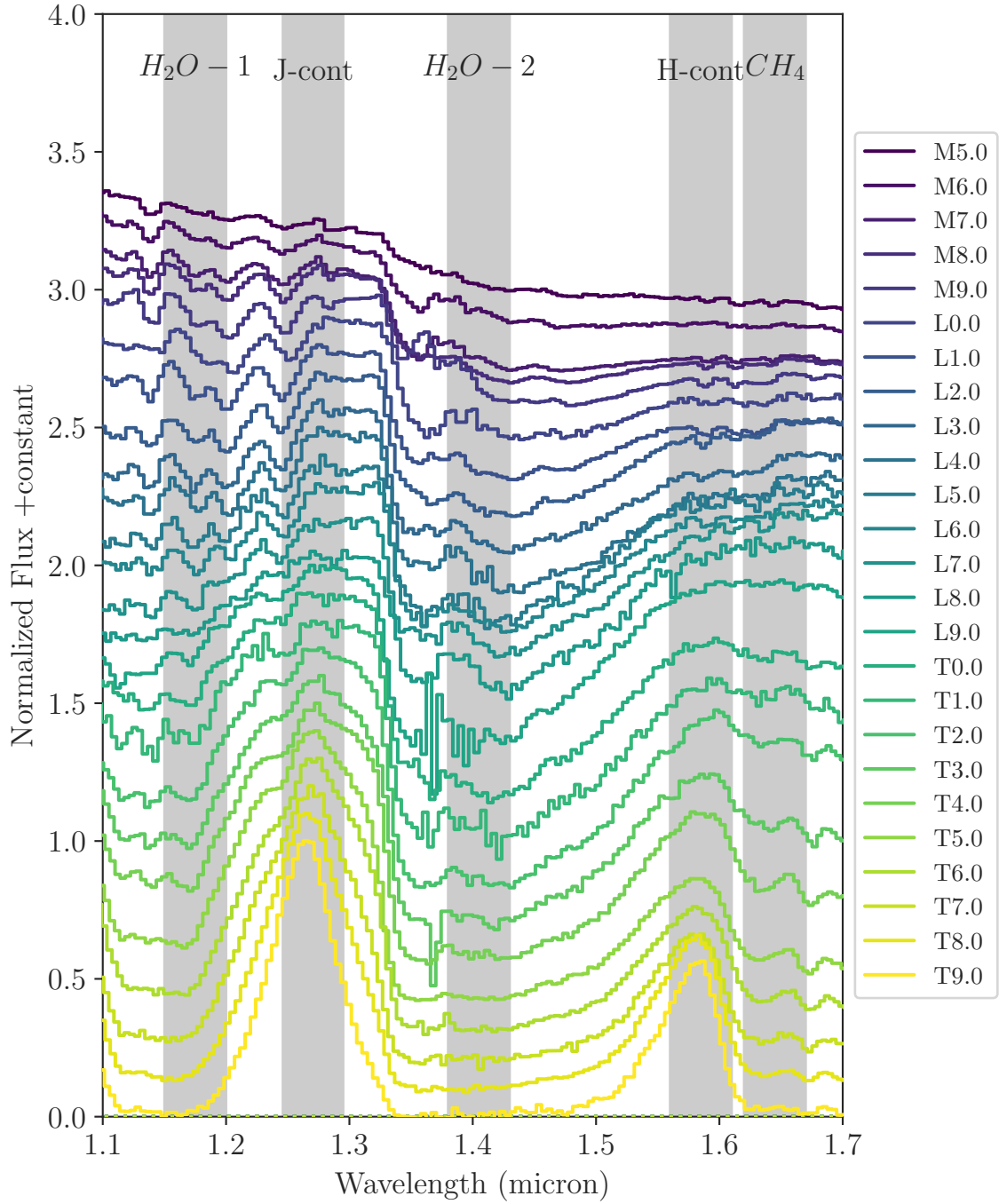


**Figure 1.** M5-T9 low resolution SpeX spectral standards (?) with highlighted bands showing the definition of spectral indices used in this study

## REFERENCES

Allers, K., Jaffe, D., Luhman, K., et al. 2007,  
 \apj, 657, 511

Atek, H., Malkan, M., McCarthy, P., et al. 2010,  
 \apj, 723, 104

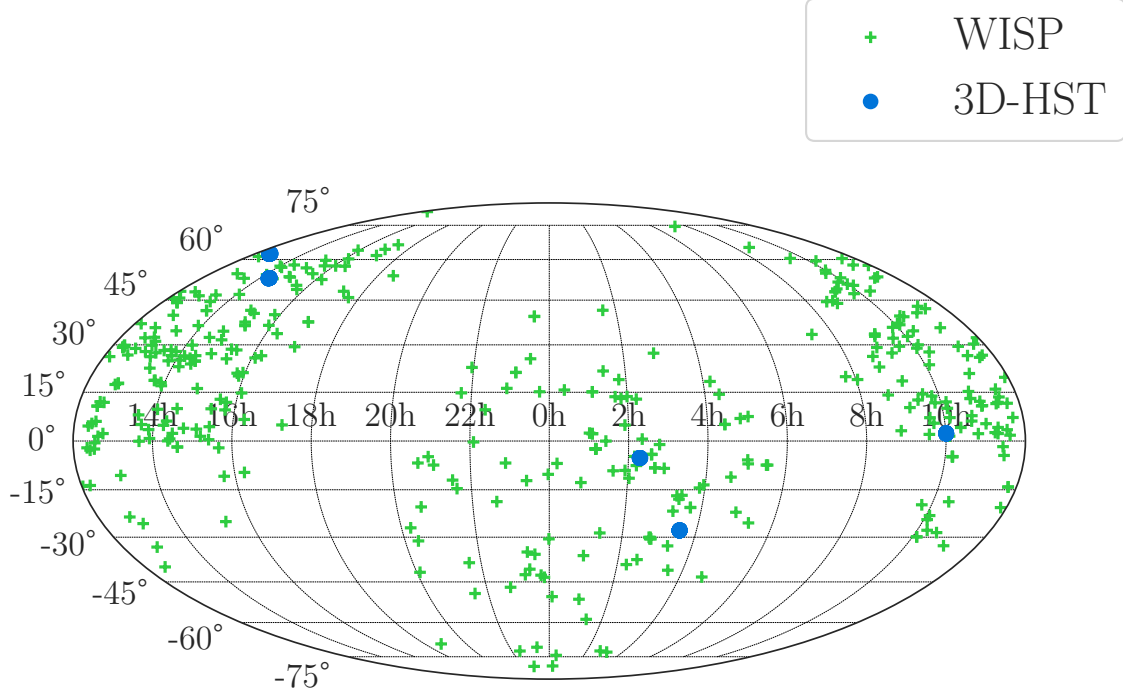


**Figure 2.** Sky map of all the pointings in WISPS and 3D-HST

- Baraffe, I., Chabrier, G., Allard, F., & Hauschildt, P. 2003, in IAU Symposium, Vol. 211, Brown Dwarfs, ed. E. Martín, 41–+
- Bardalez Gagliuffi, D., Burgasser, A., Gelino, C., et al. 2014, *\apj*, 794, 143
- Bardalez Gagliuffi, D. C., Burgasser, A. J., Schmidt, S. J., et al. 2019, arXiv e-prints, arXiv:1906.04166
- Basri, G. 1998, in Astronomical Society of the Pacific Conference Series, Vol. 134, Brown Dwarfs and Extrasolar Planets, ed. R. Rebolo, E. Martin, & M. Zapatero Osorio, 394–+
- Bastian, N., Covey, K., & Meyer, M. 2010, *\araa*, 48, 339
- Bochanski, J., Hawley, S., Covey, K., et al. 2010, *\aj*, 139, 2679
- Brammer, G., van Dokkum, P., Franx, M., et al. 2012, *\apjs*, 200, 13
- Burgasser, A. 2001, PhD thesis, AA(Department of Physics, California Institute of Technology)
- . 2004, *\apjs*, 155, 191
- . 2007, *\apj*, 659, 655
- . 2014a, ArXiv e-prints, arXiv:1406.4887



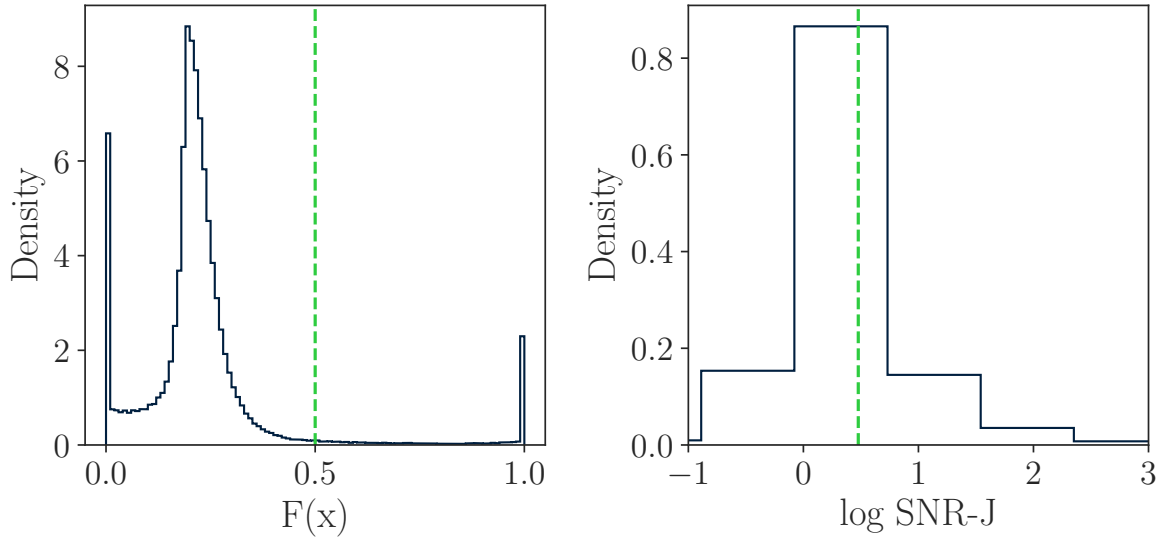


**Figure 3.** Sky map of all the pointings in WISPS and 3D-HST

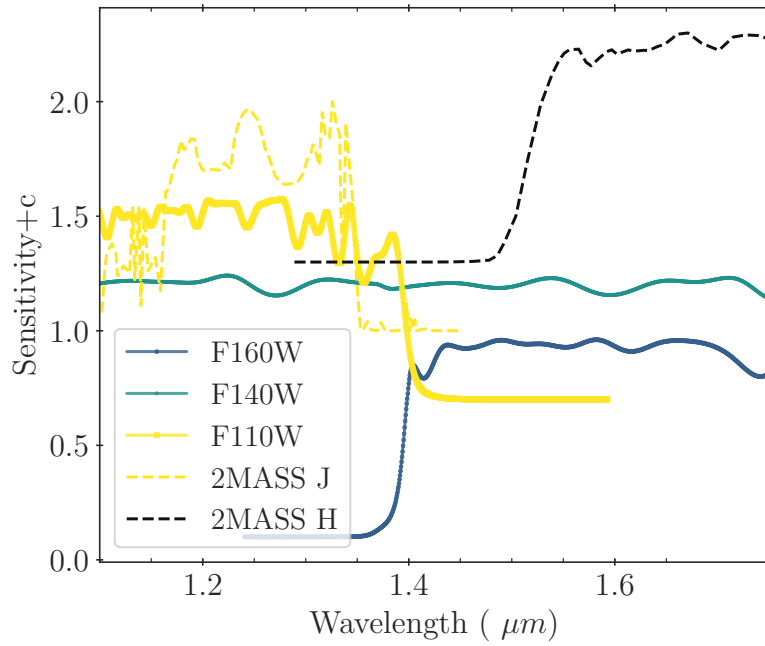


**Figure 4.** Comparison between different HST and 2MASS filters used in this study

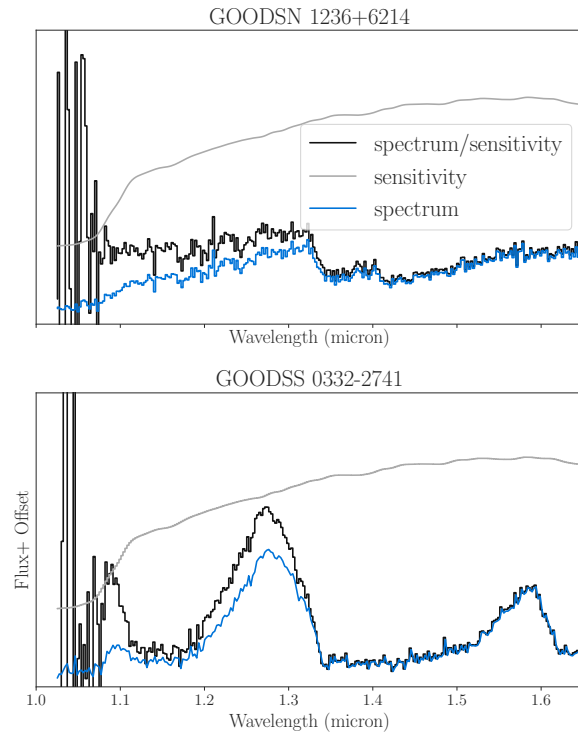


**Figure 5.** Example of 2 HST-3D spectra before and after continuum correction to obtain the correct slope. The sensitivity curve is plotted in grey.

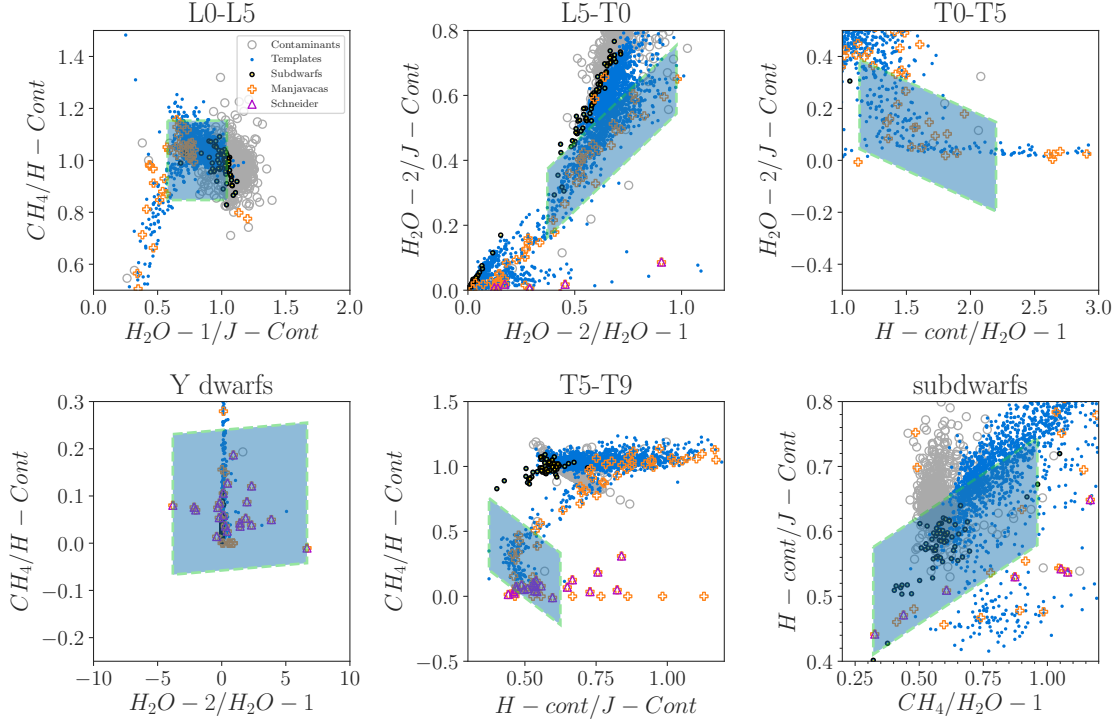


**Figure 6.** The best box selection criteria are shown from top left to bottom right for the following subtype groups: L0-L5, L5-T0, M7-L0, T0-T5, Y dwarfs and T5-T9, and subdwarfs respectively

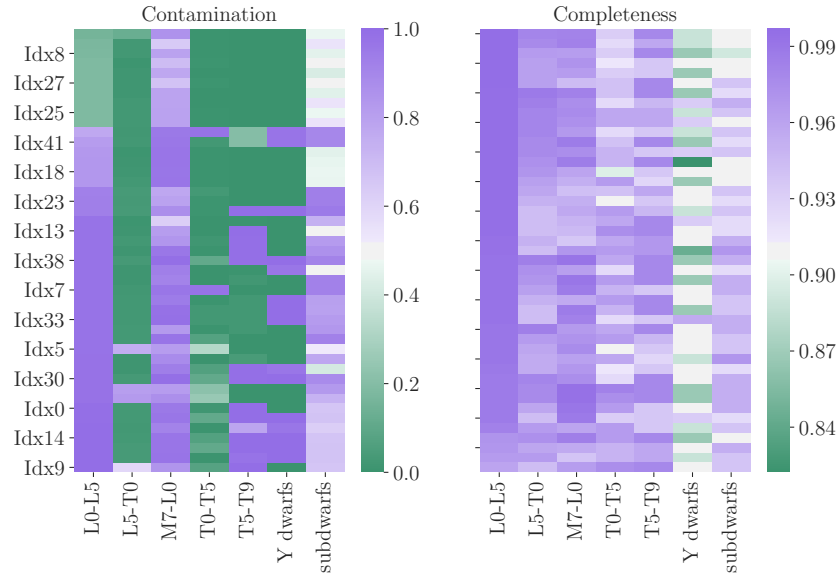


**Figure 7.** Completeness and Contamination of all indices

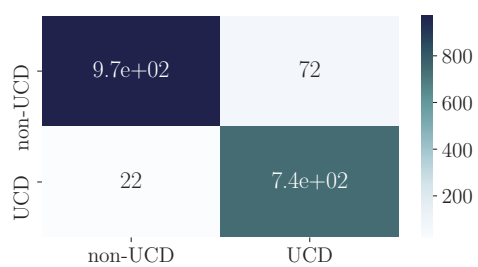


**Figure 8.** Confusion matrix for the random forest classifier used

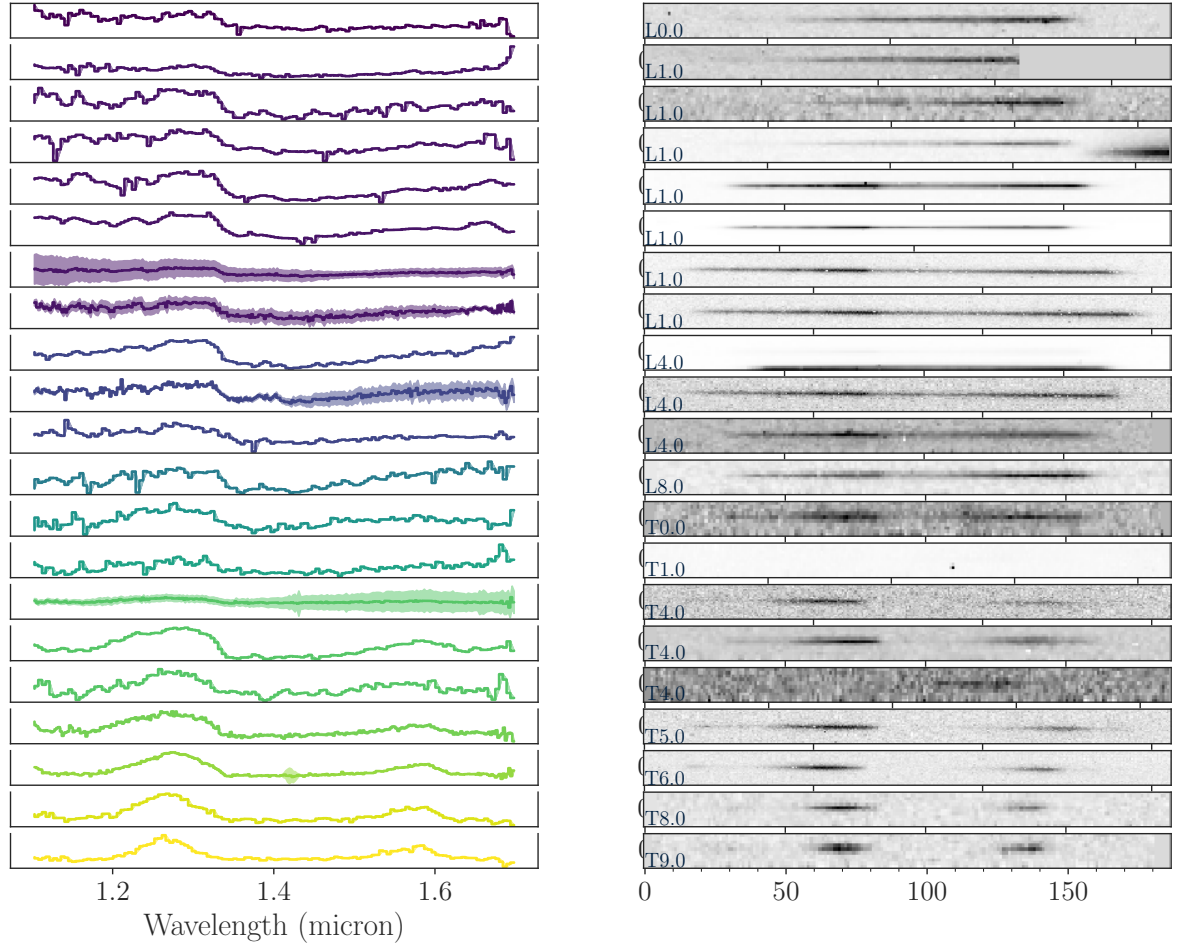


**Figure 9.** Spectral Sequence of UCDs Discovered in WISPS & 3D-HST. The right plot shows the 1D spectrum where the shaded region is the contamination exaggerated by a factor of 10, the left plot shows the cutoff of the 2d spectrum for that extracted object. The derived spectral type of each object is displayed in the left corner of the right plot

Burgasser, A., Geballe, T., Leggett, S.,  
Kirkpatrick, J., & Golimowski, D. 2006, *\apj*,  
637, 1067

Burgasser, A., Looper, D., Kirkpatrick, J., & Liu,  
M. 2007, *\apj*, 658, 557

Burgasser, A., Witte, S., Helling, C., et al. 2009,  
*\apj*, 697, 148

Burgasser, A. J. 2014b, arXiv:1406.4887

Burningham, B., Cardoso, C., Smith, L., et al.  
2013, *\mnras*, 433, 457

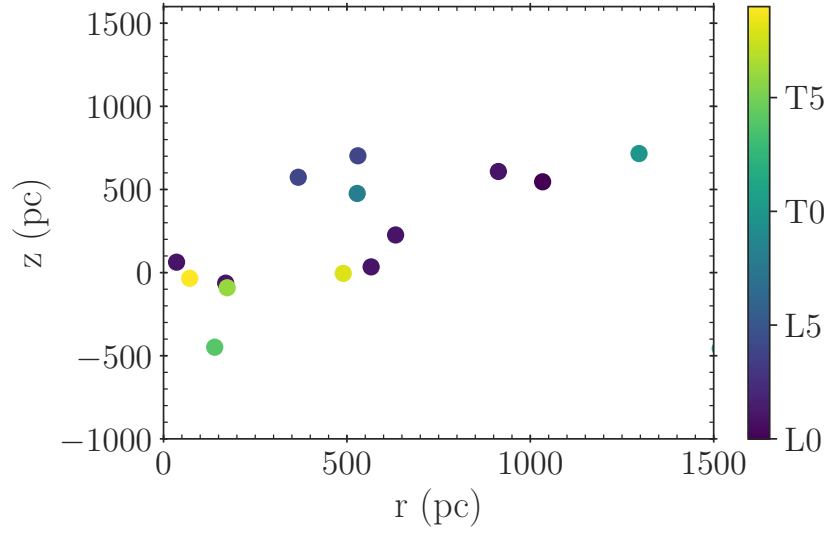


**Figure 10.** Distance distribution of UCDs Discovered in WISPS & 3D-HST

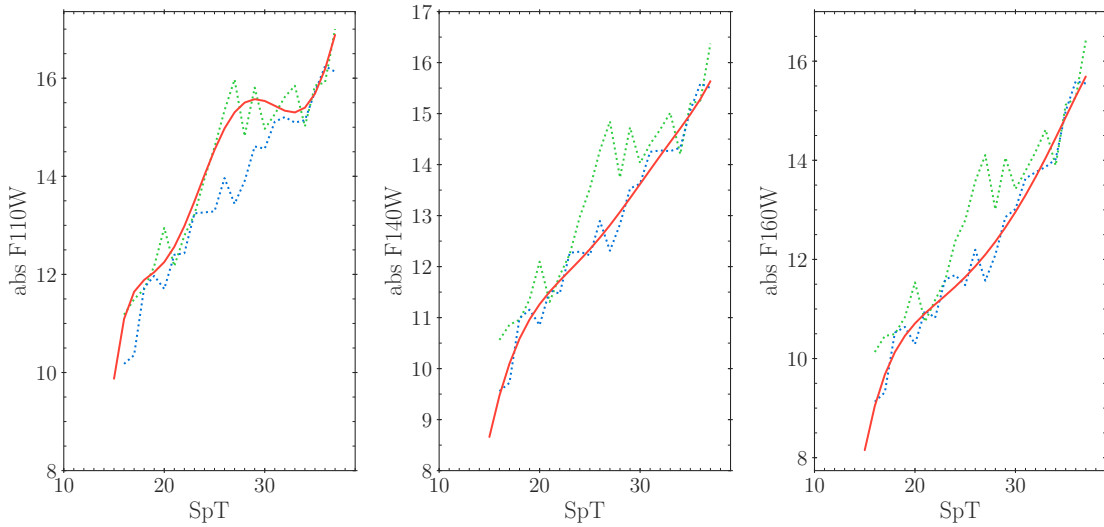


**Figure 11.** Absolute magnitude-spectral type relations for HST and 2 MASS filters. For HST filters, the dotted green curve shows the derived relation using only the offset between the respective HST filter and 2MASS J filter while the blue curve shows the derived relation using the offset with the 2MASS H filter. The solid line shows a best-fit 6th-order polynomial used, considering the wavelength coverage of the respective filters (figure ??). We report the coefficients of these polynomials in table x

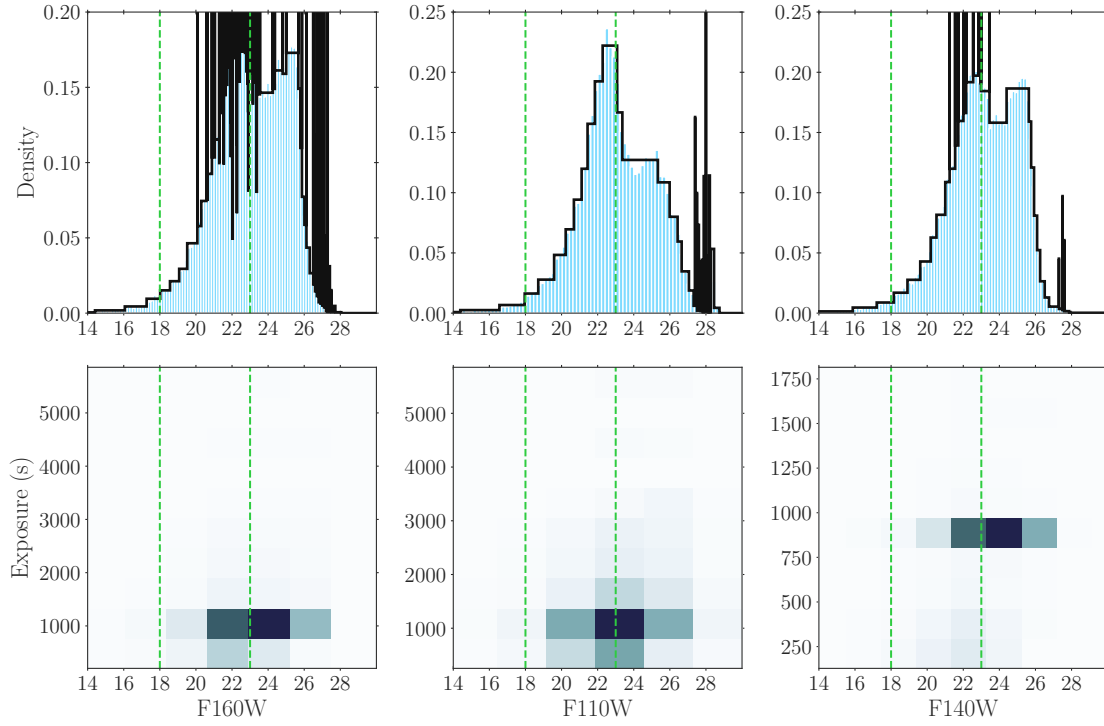


**Figure 12.** Effect of the SNR-cuts on the overall faintness limit of this study. The green vertical line shows the bright cutoff and the black line shows the faint limit. We used these limits throughout this work to estimate the effective volume

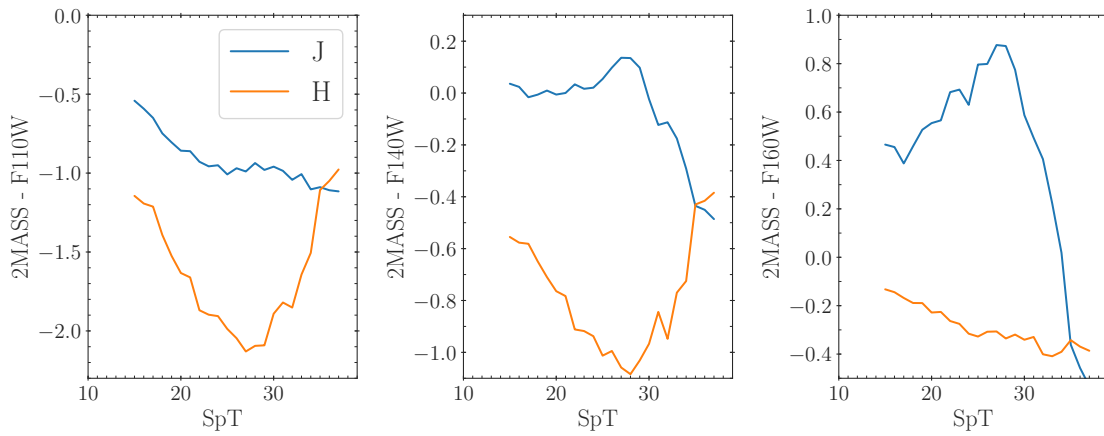


**Figure 13.** Offsets between 2MASS filters magnitudes and F110W, F140W & F160W magnitudes used to create absolute magnitude-spectral type relations for HST filters

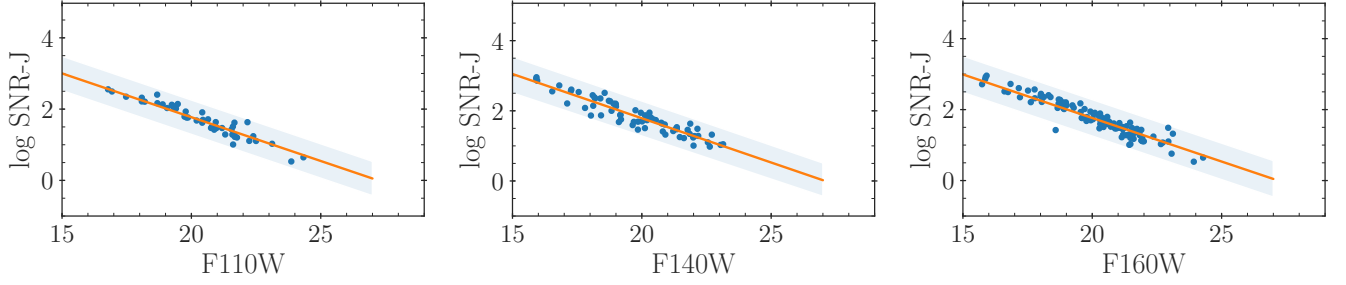


**Figure 14.** Linear fit for apparent magnitudes  $\log \text{SNR}$  for the 20 WISPS& 3D-HST UCDs used to estimate apparent magnitude for the simulated sample of UCDs

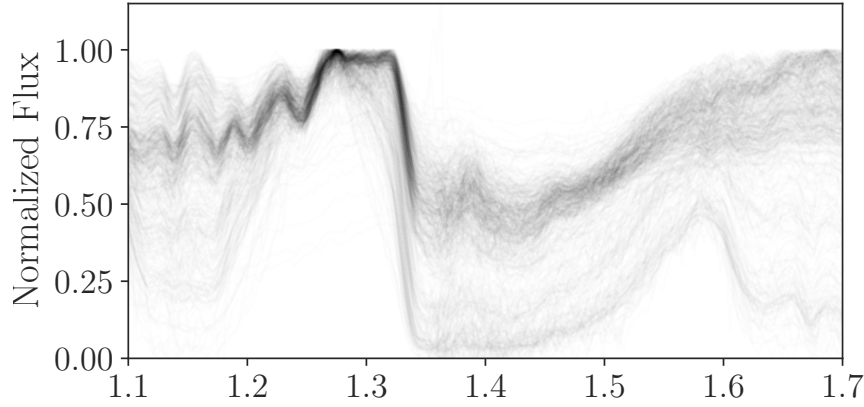


**Figure 15.** Left: Distribution of generated spectra across spectral type and SNR color-coded by their probability of selection. Right: Each spectrum is represented without binning. The dotted line shows our SNR cutoff

Burrows, A., Hubbard, W., Lunine, J., & Liebert, J. 2001, *Reviews of Modern Physics*, 73, 719

Carnero Rosell, A., Santiago, B., dal Ponte, M., et al. 2019, *arXiv e-prints*, arXiv:1903.10806

Chabrier, G. 2001, *\apj*, 554, 1274

Chabrier, G., & Baraffe, I. 2000, *\araa*, 38, 337

Chabrier, G., & Mera, D. 1997, *A&A*, 328, 83

Collaboration, T. A., Robitaille, T. P., Tollerud, E. J., et al. 2013, *arXiv:1307.6212*

Cruz, K., Reid, I., Kirkpatrick, J., et al. 2007, *\aj*, 133, 439

Cushing, M., Tokunaga, A., & Kobayashi, N. 2000, *\aj*, 119, 3019

Cushing, M., Kirkpatrick, J., Gelino, C., et al. 2011, *\apj*, 743, 50

Davis, M., Guhathakurta, P., Konidaris, N. P., et al. 2007, *The Astrophysical Journal Letters*, 660, L1



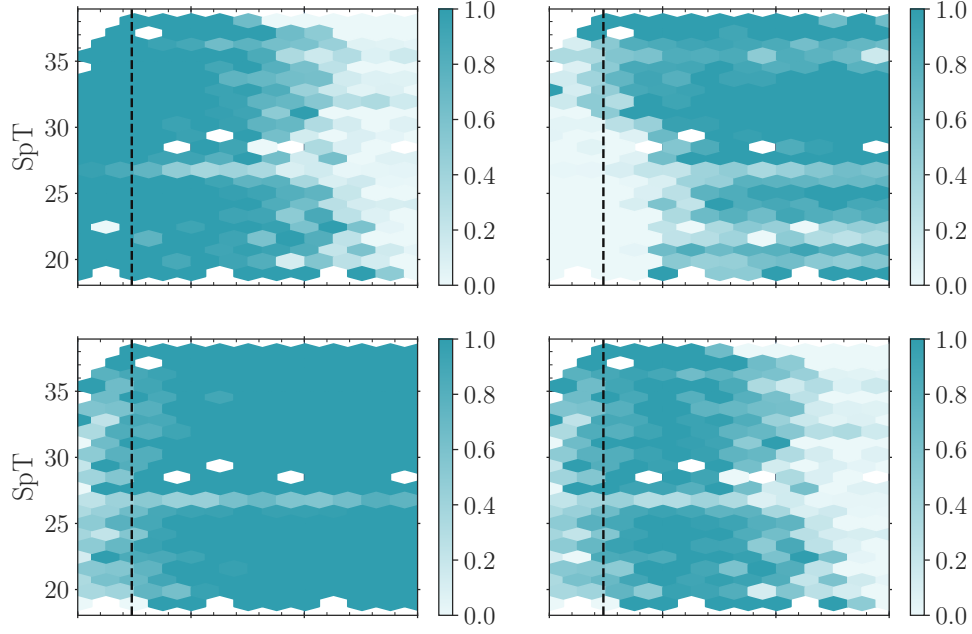


**Figure 16.** Selection probability of all the spectra used to estimate the selection function. Left: selection probability using a combination of both indices and f-test, right: selection probability using only the f-test. All SNRs are within a bin of  $\Delta \text{SNR}=3$  are assigned the same selection probability

Day-Jones, A., Marocco, F., Pinfield, D., et al.  
2013, *\mnras*, 430, 1171

Delfosse, X., Tinney, C. G., Forveille, T., et al.  
1999, *Astron. Astrophys. Suppl. Ser.*, 135, 41

Dupuy, T., & Liu, M. 2012, *\apjs*, 201, 19

Faherty, J. K., Bochanski, J. J., Gagne, J., et al.  
2018, *The Astrophysical Journal*, 863, 91

Filippazzo, J. C., Rice, E. L., Faherty, J., et al.  
2015, *Astrophysical Journal*, 810, 158

Gagné, J., Faherty, J. K., Cruz, K. L., et al. 2015,  
*arXiv:1506.07712*

Giavalisco, M., Ferguson, H. C., Koekemoer,  
A. M., et al. 2004, *The Astrophysical Journal*,  
600, L93

Gould, A., Bahcall, J., & Flynn, C. 1997, *\apj*,  
482, 913

Hardegree-Ullman, K. K., Cushing, M. C.,  
Muirhead, P. S., & Christiansen, J. L. 2019,  
*arXiv e-prints*, *arXiv:1905.05900*

Hogg, D. W., Bovy, J., & Lang, D. 2010,  
*arXiv:1008.4686*

Holwerda, B. W., Trenti, M., Clarkson, W., et al.  
2014, *The Astrophysical Journal*, 788, 77

Jones, E., Oliphant, T., Peterson, P., et al. 2001–,  
*SciPy: Open source scientific tools for Python*, ,  
[Online; accessed *jtoday*]

Jurić, M., Ivezić, Ž., Brooks, A., et al. 2008, *\apj*,  
673, 864

Kerins, E. J. 1997, *A&A*, 328, 5

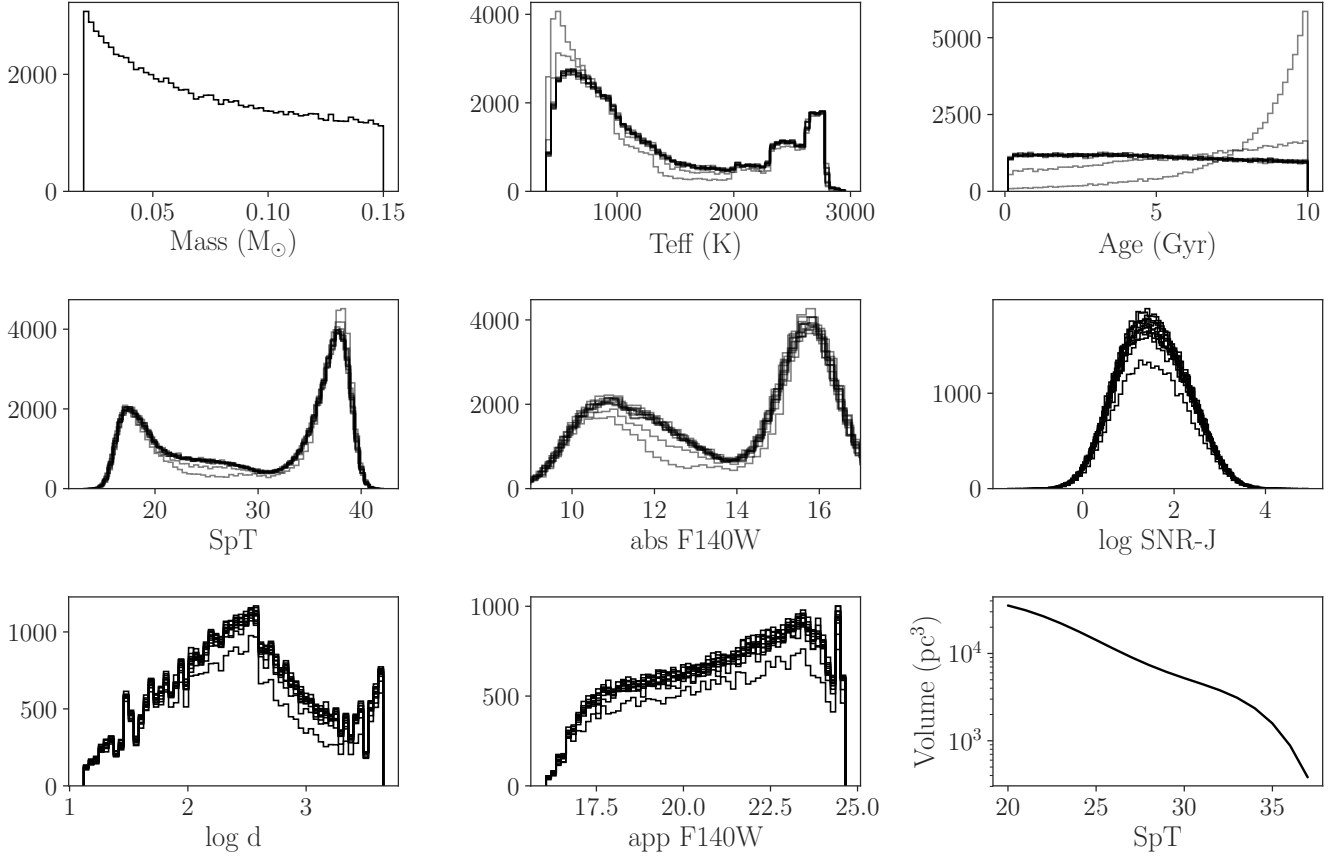


**Figure 17.** Distribution of parameters of the simulated sample of UCDs

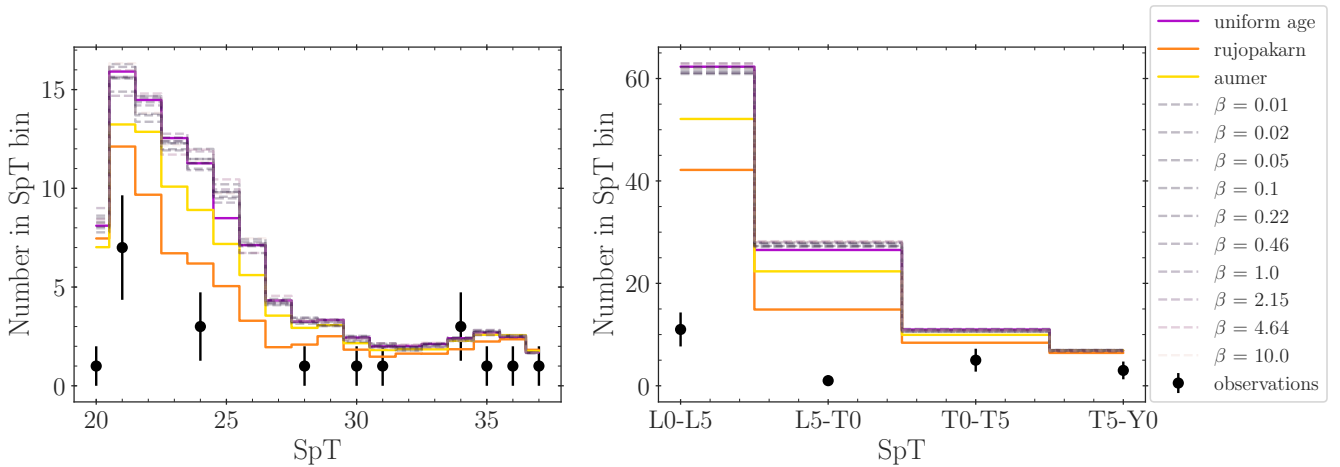


**Figure 18.** Distribution of UCDs found in all 533 pointings of HST & 3D-HST compared to the expected number. There is an agreement with the late type objects but we over-predict the number of L dwarfs

- Kimble, R. A., MacKenty, J. W., O’Connell, R. W., & Townsend, J. A. 2008, Wide Field Camera 3: a powerful new imager for the Hubble Space Telescope, , , doi:10.1117/12.789581
- Kirkpatrick, J. 2005, *\araa*, 43, 195
- Kirkpatrick, J., Looper, D., Burgasser, A., et al. 2010, *\apjs*, 190, 100
- Kirkpatrick, J., Cushing, M., Gelino, C., et al. 2011, *\apjs*, 197, 19
- Kirkpatrick, J. D., Reid, I. N., Liebert, J., et al. 2000, *The Astronomical Journal*, 120, 447
- Kirkpatrick, J. D., Martin, E. C., Smart, R. L., et al. 2019, *ApJS*, 240, 19
- Kümmel, M., Walsh, J. R., Pirzkal, N., Kuntschner, H., & Pasquali, A. 2009, *Publications of the Astronomical Society of the Pacific*, 121, 59
- Kuntschner, H., Kümmel, M., & Walsh, J. R. 2013
- Lawrence, A., & Others. 2007, *\mnras*, 379, 1599
- Lodieu, N., Espinoza Contreras, M., Zapatero Osorio, M. R., et al. 2017, *Astronomy & Astrophysics*, 598, A92
- Lopez-Santiago, J., Montes, D., Crespo-Chacon, I., & Fernandez-Figueroa, M. J. 2006, *The Astrophysical Journal*, 643, 1160
- LSST Science Collaboration, L. S., Abell, P. A., Allison, J., et al. 2009, arXiv:0912.0201
- Luhman, K. L., & Mamajek, E. E. 2012, *The Astrophysical Journal*, 758, 31
- Mamajek, E. E. 2015, *Proceedings of the International Astronomical Union*, 10, 21
- Manjavacas, E., Apai, D., Zhou, Y., et al. 2018, arXiv:1812.03963
- Marocco, F., Jones, H. R. A., Day-Jones, A. C., et al. 2015, *Monthly Notices of the Royal Astronomical Society*, 449, 3651
- Martin, E. C., Mace, G. N., McLean, I. S., et al. 2017, *The Astrophysical Journal*, 838, 73
- Masters, D., McCarthy, P., Burgasser, A., et al. 2012, *\apjl*, 752, L14
- Metchev, S., Kirkpatrick, J., Berriman, G., & Looper, D. 2008, *\apj*, 676, 1281
- Momcheva, I. G., Brammer, G. B., van Dokkum, P. G., et al. 2016, *The Astrophysical Journal Supplement Series*, 225, 27
- Pedregosa, F., Varoquaux, G., Gramfort, A., et al. 2012, arXiv e-prints, arXiv:1201.0490
- Pirzkal, N., Sahu, K., Burgasser, A., et al. 2005, *\apj*, 622, 319
- Pirzkal, N., Burgasser, A., Malhotra, S., et al. 2009, *\apj*, 695, 1591
- Reid, I., Kirkpatrick, J., Liebert, J., et al. 1999, *\apj*, 521, 613
- Reylé, C. 2018, *Astronomy & Astrophysics*, 619, L8
- Reylé, C., & Robin, A. C. 2001, *A&A*, 373, 886
- Reyle, C., Delorme, P., Willott, C. J., et al. 2010, *Astronomy and Astrophysics*, Volume 522, id.A112, 15 pp., 522, arXiv:1008.2301
- Ryan, R. E., Thorman, P. A., Yan, H., et al. 2011, *The Astrophysical Journal*, 739, 83
- Ryan, R. E., Thorman, P. A., Schmidt, S. J., et al. 2017, *The Astrophysical Journal*, 847, 53

- Ryan Jr., R., Hathi, N., Cohen, S., & Windhorst, R. 2005, *\apjl*, 631, L159
- Ryan Jr., R. E., & Reid, I. N. 2016, *The Astronomical Journal*, 151, 92
- Schneider, A. C., Cushing, M. C., Kirkpatrick, J. D., et al. 2015, *The Astrophysical Journal*, 804, 92
- Scoville, N., Aussel, H., Brusa, M., et al. 2007, *The Astrophysical Journal Supplement Series*, 172, 1
- Skelton, R. E., Whitaker, K. E., Momcheva, I. G., et al. 2014, *The Astrophysical Journal Supplement Series*, 214, 24
- Sorahana, S., Nakajima, T., & Matsuoka, Y. 2018, *arXiv:1811.07496*
- Spergel, D., Gehrels, N., Baltay, C., et al. 2015, *arXiv:1503.03757*
- Tokunaga, A., & Kobayashi, N. 1999, *\aj*, 117, 1010
- Van Vledder, I., Van Der Vlugt, D., Holwerda, B. W., et al. 2016, *Monthly Notices of the Royal Astronomical Society*, 458, 425
- Zhang, Z. H., Burgasser, A. J., Gálvez-Ortiz, M. C., et al. 2019, *MNRAS*, 486, 1260